

InfScene-SR: Spatially Continuous Inference for Arbitrary-Size Image Super-Resolution

Shoukun Sun¹, Zhe Wang², Xiang Que³, Jiyin Zhang¹, and Xiaogang Ma¹

¹ Computer Science Department,
University of Idaho, Moscow, Idaho, USA
{ssun, jiyinz, max}@uidaho.edu

² College of Computer and Information Sciences,
Fujian Agriculture and Forestry University, China
quexiang@fafu.edu.cn

³ National Center for Ecological Analysis and Synthesis (NCEAS),
University of California Santa Barbara, Santa Barbara, California, USA
zwang@nceas.ucsb.edu

Abstract. Image Super-Resolution (SR) aims to recover high-resolution (HR) details from low-resolution (LR) inputs, a task where Denoising Diffusion Probabilistic Models (DDPMs) have recently shown superior performance compared to Generative Adversarial Networks (GANs) based approaches. However, standard diffusion-based SR models, such as SR3, are typically trained on fixed-size patches and struggle to scale to arbitrary-sized images due to memory constraints. Applying these models via independent patch processing leads to visible seams and inconsistent textures across boundaries. In this paper, we propose InfScene-SR, a framework enabling spatially continuous super-resolution for large, arbitrary scenes. We adapt the iterative refinement process of diffusion models with a novel guided and variance-corrected fusion mechanism, allowing for the seamless generation of large-scale high-resolution imagery without retraining. We validate our approach on remote sensing datasets, demonstrating that InfScene-SR not only reconstructs fine details with high perceptual quality but also eliminates boundary artifacts, benefiting downstream tasks such as semantic segmentation.

Keywords: Super-resolution · Diffusion Models · Image Processing · Deep Learning

1 Introduction

Super-Resolution (SR) is a fundamental problem in computer vision, aiming to reconstruct a high-resolution (HR) image from a low-resolution (LR) observation. It has critical applications in diverse fields, ranging from medical imaging and surveillance to remote sensing, where detailed imagery is essential for analysis. Traditional interpolation methods (e.g., bicubic) and early deep learning approaches based on Convolutional Neural Networks (CNNs) often yield overly smooth textures. Generative Adversarial Networks (GANs) [2] improved perceptual quality but are prone to mode collapse and training instability.

Recently, Denoising Diffusion Probabilistic Models (DDPMs) [5] have emerged as a powerful class of generative models, outperforming GANs in image synthesis and restoration. Methods like Super-Resolution via Repeated Refinement (SR3) [9] formulate SR as a conditional image generation task, iteratively refining noise into a high-resolution image conditioned on the LR input. These methods demonstrate an unprecedented ability to hallucinate realistic high-frequency details.

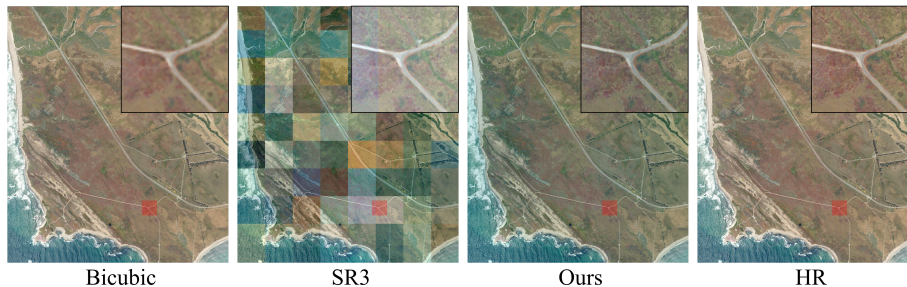


Fig. 1: Visual comparison of super-resolution methods. The proposed InfScene-SR reconstruction eliminates the grid artifacts visible in the standard SR3 output while recovering fine details superior to bicubic interpolation.

However, a major limitation of current diffusion-based SR models is their restriction to fixed-size input patches (e.g., 64×64 or 256×256) due to the quadratic memory complexity of attention mechanisms and limited GPU memory. This poses a challenge for real-world applications like satellite imagery analysis, which involves arbitrary-sized, gigapixel-scale images. The standard workaround—processing an image as a grid of independent patches—fails for diffusion models. Unlike deterministic CNNs, the stochastic nature of the diffusion reverse process leads to disjointed content and visible seams at patch boundaries, disrupting the spatial continuity required for large-scene understanding.

To address this, we present InfScene-SR, a method for spatially continuous inference on arbitrary-sized images using pre-trained diffusion models. Drawing inspiration from recent advances in large-content generation [10], we introduce a fusion strategy during the iterative reverse diffusion steps. By coordinating the noise prediction across overlapping patches using guided and variance-corrected fusion, our method enforces global consistency while preserving the local detail generation capability of the base SR3 model.

Our contributions are as follows:

- We propose InfScene-SR, a diffusion-based super-resolution framework capable of handling arbitrary-sized scenes without retraining.
- We integrate a guided and variance-corrected fusion mechanism into the SR3 inference process to eliminate patch boundary artifacts.

- We demonstrate the effectiveness of our approach on large-scale remote sensing data, showing improvements in both visual quality and downstream semantic segmentation performance.

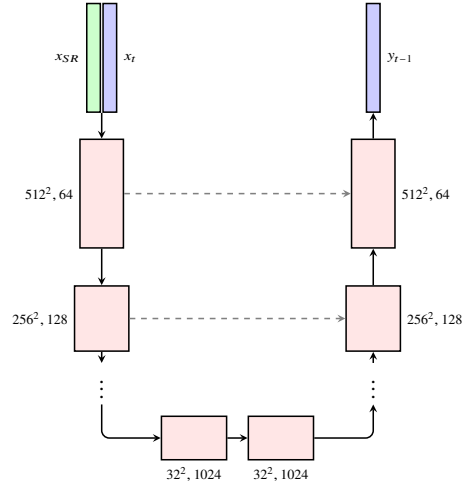


Fig. 2: Detailed U-Net architecture of the SR3 backbone. The network concatenates the super-resolution condition x_{SR} and noisy latent x_t , processing them through a symmetric encoder-decoder structure with attention bottlenecks to predict the noise component y_{t-1} .

2 Related Work

2.1 Image Super-Resolution

Deep learning has revolutionized Single Image Super-Resolution (SISR). Early methods like SRCNN learned end-to-end mappings from LR to HR spaces. Subsequent architectures introduced residual blocks (ResNet), dense connections (DenseNet), and attention mechanisms to improve reconstruction fidelity. To tackle the issue of blurry textures associated with Mean Squared Error (MSE) loss, GAN-based methods such as SRGAN and ESRGAN introduced adversarial losses, encouraging the generation of photo-realistic textures. Despite their success, GANs can suffer from training instability and generation artifacts.

2.2 Diffusion Models for Super-Resolution

Diffusion models have recently set new benchmarks in generative modeling. Ho et al. [5] introduced Denoising Diffusion Probabilistic Models (DDPMs), which learn to reverse a gradual noising process. Saharia et al. adapted this for super-resolution in SR3 [9], conditioning the reverse process on the LR image. SR3 demonstrated that diffusion models

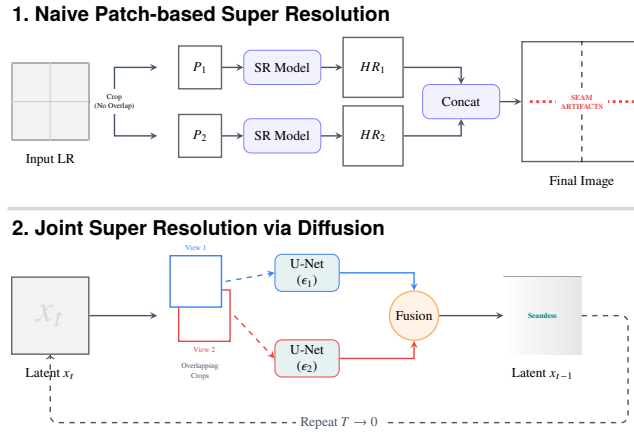


Fig. 3: Comparison of inference pipelines. Top: Naive patch-based processing leads to boundary seams. Bottom: The proposed InfScene-SR pipeline employs a joint diffusion strategy with overlapping views and a fusion mechanism to ensure global spatial continuity.

could outperform regression and GAN-based baselines in human evaluation. Subsequent works have focused on improving sampling speed and conditioning mechanisms, but most assume fixed-size inputs.

2.3 Large-Content Image Generation

Generating or processing images beyond the training crop size is a challenge. Autoregressive models generate pixels sequentially but are computationally expensive. In the context of diffusion models, recent works have explored patch-based generation. SyncDiffusion attempts to synchronize the gradient updates of patches. More recently, Sun et al. [10] proposed a guided and variance-corrected fusion approach for large-content generation. This method aligns the mean and variance of overlapping regions in the latent feature space during the reverse process, ensuring seamless transitions. Our work extends these concepts to the conditional setting of SR, enabling the application of SR3 to large-scale geospatial imagery.

3 Proposed Method

We propose **InfScene-SR**, a unified framework designed to enforce spatial continuity and statistical consistency for arbitrary-scale image super-resolution. Our approach is founded on a dual-constraint analysis of the conditional diffusion generation process: the stochastic integrity of the reverse trajectory and the computational tractability of global spatial fusion. In this section, we first analyze the stochastic evolution characteristics of the SR3 model under γ -parameterization, theoretically deriving the *Variance Erosion* phenomenon caused by multi-view fusion. Subsequently, we introduce **Memory-Decoupled Accumulation (MDA)**, a mathematically equivalent but computationally orthogonal algorithm that enables parallelized, infinite-resolution inference.



Fig. 4: Geographic extent of the study area. The dataset covers 15 coastal counties in California using 2024 NAIP imagery, with Santa Barbara County (highlighted) reserved for testing.

3.1 Preliminaries: γ -Parameterized Reverse Diffusion

We adopt the SR3 framework [9] as our generative backbone. The super-resolution process is modeled as a conditional reverse Markov chain, iteratively refining a pure Gaussian noise distribution $y_T \sim \mathcal{N}(0, I)$ into a high-resolution image y_0 conditioned on a low-resolution input x .

The diffusion process in SR3 is defined by a scalar hyperparameter schedule γ , representing the signal-to-noise ratio. In the inference phase at timestep t , the single-step update (formulated via Langevin dynamics) is given by:

$$y_{t-1} = \frac{1}{\sqrt{\alpha_t}} \left(y_t - \frac{1 - \alpha_t}{\sqrt{1 - \gamma_t}} f_\theta(x, y_t, \gamma_t) \right) + \sqrt{1 - \alpha_t} \mathbf{z}_t, \quad (1)$$

where f_θ is the denoising neural network, $\alpha_t = \gamma_t / \gamma_{t-1}$ controls the noise injection ratio, and $\mathbf{z}_t \sim \mathcal{N}(0, I)$ represents the standard Gaussian noise term.

To simplify the derivation, we denote the deterministic component of the update as $\mathcal{D}_\theta(y_t, x, \gamma_t)$. Consequently, Eq. 1 can be reformulated as:

$$y_{t-1} = \mathcal{D}_\theta(y_t, x, \gamma_t) + \sigma_{target} \mathbf{z}_t, \quad (2)$$

where $\sigma_{target} = \sqrt{1 - \alpha_t}$. This formulation explicitly indicates that the high-frequency texture details generated by the model are governed by the variance of the stochastic term.

However, a critical limitation arises from the architectural constraints of diffusion models, which are typically restricted to processing fixed-size inputs. Training a universal

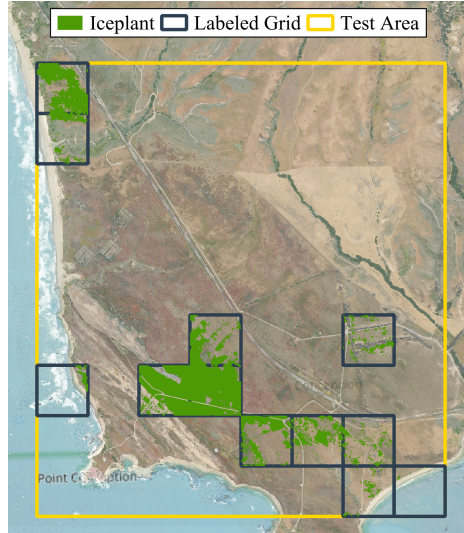


Fig. 5: Downstream task overview: Semantic segmentation of the invasive *Carpobrotus edulis* (Iceplant). The goal is to delineate Iceplant coverage from aerial imagery, comparing performance across original and super-resolved inputs.

model capable of directly handling arbitrary or ultra-large-scale images is computationally prohibitive. Consequently, when applying deep learning-based super-resolution to large geospatial scenes, the standard practice necessitates partitioning the image into independent patches. This fragmentation, however, is problematic for stochastic generative models. Due to the diffusion process’s high sensitivity to the initial random noise \mathbf{z}_T and the localized effective receptive field, independently generated adjacent patches often exhibit semantic discontinuities and style drift, even when the underlying semantic content is continuous.

3.2 Derivation of Gamma-Dependent Variance Erosion

When extending the diffusion prior to arbitrary-scale scenes, the global panorama Y is reconstructed by fusing a set of overlapping local patches $\{y^{(k)}\}_{k \in \Omega}$. For any pixel coordinate \mathbf{p} in the global canvas, its value is determined by the expectation of all covering patches.

Let $\omega_k(\mathbf{p})$ denote the spatial guidance weight for the k -th patch. A naive linear fusion strategy leads to the following update rule:

$$Y_{t-1}(\mathbf{p}) = \frac{\sum_k \omega_k(\mathbf{p}) \mathcal{D}_\theta^{(k)}}{\sum_k \omega_k(\mathbf{p})} + \frac{\sum_k \omega_k(\mathbf{p}) \sigma_{target} \mathbf{z}_t^{(k)}}{\sum_k \omega_k(\mathbf{p})}. \quad (3)$$

While the deterministic term \mathcal{D}_θ ensures semantic consistency across boundaries, the statistical properties of the stochastic term undergo a fundamental shift. Since the noise samples $\mathbf{z}_t^{(k)}$ from different patches are independent and identically distributed

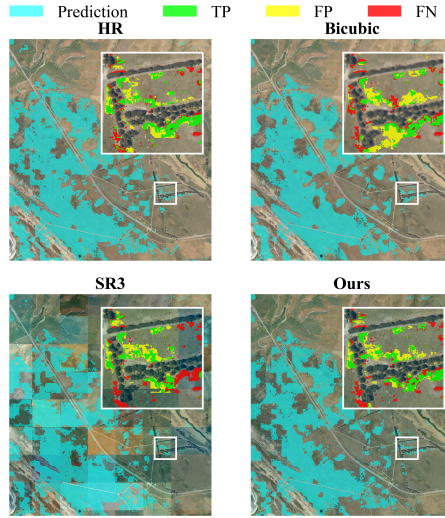


Fig. 6: Qualitative results for Iceplant segmentation. InfScene-SR (ours) produces segmentation maps with boundary precision closer to the High-Resolution ground truth compared to other upsampling methods.

(i.i.d.) variables from $\mathcal{N}(0, I)$, the variance of the fused noise term, denoted as Σ_{fused}^2 , becomes:

$$\Sigma_{fused}^2(\mathbf{p}) = \sigma_{target}^2 \cdot \frac{\sum_k \omega_k(\mathbf{p})^2}{\underbrace{(\sum_k \omega_k(\mathbf{p}))^2}_{\lambda(\mathbf{p})}}. \quad (4)$$

We define $\lambda(\mathbf{p})$ as the **Variance Erosion Factor**. According to the Cauchy-Schwarz inequality, $\lambda(\mathbf{p}) \leq 1$, with equality holding only in non-overlapping regions. This derivation proves that under the γ -schedule of SR3, the stochastic perturbations in overlapping regions are inevitably suppressed. We term this phenomenon **Gamma-Dependent Variance Erosion**. It results in a spectral shift towards low frequencies, manifesting as blurring and texture loss in the fused regions.

To rectify this theoretical deviation, we derive a **Gamma-Corrected Projection** for the fused latent variable:

$$Y_{t-1}^*(\mathbf{p}) = \frac{Y_{t-1}(\mathbf{p}) - \bar{\mu}(\mathbf{p})}{\sqrt{\lambda(\mathbf{p})}} + \bar{\mu}(\mathbf{p}), \quad (5)$$

where $\bar{\mu}(\mathbf{p}) = \frac{\sum \omega_k \mathcal{D}_\theta^{(k)}}{\sum \omega_k}$ represents the mean manifold of the deterministic components.

3.3 Memory-Decoupled Accumulation (MDA)

Although Eq. 5 theoretically restores the variance, its direct implementation poses a severe engineering bottleneck. The calculation of $\lambda(\mathbf{p})$ and $\bar{\mu}(\mathbf{p})$ necessitates global

normalization terms $W(\mathbf{p}) = \sum \omega_k$ and $S(\mathbf{p}) = \sqrt{\sum \omega_k^2}$. This implies a *Global-Hold Dependency*, requiring the entire panoramic tensor $Y \in \mathbb{R}^{H \times W \times C}$ to be loaded into memory before normalization can occur. For gigapixel-level remote sensing imagery, this requirement makes the algorithm computationally intractable on standard hardware.

To resolve this scalability constraint, we propose **Memory-Decoupled Accumulation (MDA)**. We observe that through algebraic factorization, Eq. 5 can be decomposed into **Patch-Independent Affine Operators**, thereby eliminating the dependency on the global state.

Operator Factorization By expanding and regrouping the terms in Eq. 5, we define a local operator Ψ_k specific to the k -th patch. For any local pixel \mathbf{p}_{loc} within the patch, its contribution to the global update can be pre-calculated as:

$$\Psi_k \left(y_{t-1}^{(k)}, \mathcal{D}_\theta^{(k)}; \mathbf{p} \right) = \underbrace{\frac{\omega_k(\mathbf{p})}{S(\mathbf{p})}}_{\text{Gain Term}} \cdot y_{t-1}^{(k)} + \omega_k(\mathbf{p}) \underbrace{\left(\frac{1}{W(\mathbf{p})} - \frac{1}{S(\mathbf{p})} \right)}_{\text{Shift Term}} \cdot \mathcal{D}_\theta^{(k)}. \quad (6)$$

Here, the *Gain Term* is responsible for restoring the variance eroded by $\lambda(\mathbf{p})$, while the *Shift Term* corrects the mean shift introduced by the re-scaling process. Crucially, since the patch stride and overlap patterns are predetermined, the normalization fields $W(\mathbf{p})$ and $S(\mathbf{p})$ exhibit strict **Translational Periodicity**. Consequently, the coefficient maps for the Gain and Shift terms can be pre-computed as small periodic tensors $\mathbf{T}_{gain}, \mathbf{T}_{shift} \in \mathbb{R}^{h \times w}$ (where h, w are the patch dimensions) and reused across the entire inference process.

Parallelized Stream Inference Leveraging the MDA formulation, we restructure the global SR3 inference into a fully parallelized, streaming process. The global image reconstruction degenerates into a stateless accumulation:

$$Y_{t-1}^*(\mathbf{p}) = \sum_{k \in \Omega_p} \Psi_k \left(y_{t-1}^{(k)}, \mathcal{D}_\theta^{(k)} \right). \quad (7)$$

This reformulation yields two critical advantages:

- **$O(1)$ Memory Complexity:** The inference engine is only required to maintain the memory overhead for a single patch, independent of the target image’s total resolution (H, W) . This effectively enables *Infinite-Resolution* inference on consumer-grade GPUs.
- **Operator Atomicity:** Each Ψ_k operation is independent. This allows for asynchronous inference on distributed computing clusters for different geographical tiles, which can be seamlessly merged via simple summation without post-processing.

4 Experiments

4.1 Datasets

We evaluate our method on two distinct remote sensing datasets, chosen to reflect real-world resolution differences and downstream applications. Remote sensing imagery

constitutes a particularly compelling benchmark for spatially continuous SR, as geospatial analysis fundamentally operates on seamless, scene-level reconstructions rather than disjoint patches. Patch-based processing fractures spatially continuous ground objects—such as buildings, roads, and vegetation canopies—across tile boundaries. In downstream tasks that rely on the identification and delineation of these objects, such discontinuities can introduce systematic errors in both geometric and semantic accuracy. Consequently, this domain provides a rigorous testbed for evaluating the spatial coherence enforced by our fusion mechanism. A summary of dataset statistics is provided in Table 1.

Super Resolution Dataset The primary dataset for SR model training consists of imagery from the National Agriculture Imagery Program (NAIP) [12] gathered in 2024, covering the coastal counties of California (Figure 4).

- **Setup:** We simulate a $5\times$ super-resolution task, upscaling from 3m to 0.6m ground sample distance. This configuration targets a practically significant resolution gap: enhancing Planet [7] satellite imagery to the spatial quality of NAIP orthophotography. While NAIP provides sub-meter resolution, its acquisition cycle of 2–3 years severely limits temporal analysis. Planet constellations, by contrast, offer near-daily global revisits but at a coarser 3m resolution. By bridging this resolution–revisit trade-off through learned super-resolution, our framework effectively upgrades daily Planet observations to NAIP-equivalent detail, unlocking high-frequency temporal monitoring at high spatial fidelity—a capability critical for time-sensitive applications such as agricultural phenology tracking, disaster response, and rapid land-cover change detection.
- **Coverage:** The dataset spans 15 coastal counties in California state. Santa Barbara County serves as the held-out test area. For the remaining counties, a 10 km buffer zone extending inland from the ocean boundary defines the coastal extraction region. Patches are discarded if their spatial overlap with this buffer zone is below 90% or if they contain more than 10% invalid pixels.
- **Statistics:** The dataset comprises 248,730 patches of size 512×512 using the first three spectral bands (RGB), split into 236,633 training, 8,569 validation, and 3,528 test patches.

Iceplant Segmentation Dataset To assess downstream task performance, we utilize a semantic segmentation dataset targeting the detection of *Carpobrotus edulis* (Iceplant), an aggressive invasive species that displaces native vegetation along the California coastline (Figure 5). Active eradication and monitoring campaigns require accurate, spatially explicit mapping of Iceplant coverage, making this a well-motivated real-world benchmark for evaluating the practical utility of super-resolved imagery. Crucially, this task also highlights the temporal dimension of our SR framework: relying solely on native NAIP imagery restricts monitoring to the program’s 2–3 year acquisition cycle, which is insufficient for tracking the rapid seasonal spread and regrowth patterns characteristic of invasive species. By applying our SR model to daily Planet observations, land managers could potentially conduct annual or even seasonal assessments at sub-meter resolution, enabling more timely and adaptive conservation interventions.

- **Location:** Santa Barbara County, CA.
- **Data Split:** The training set consists of 4,913 patches (128×128) from 2022 NAIP imagery. The test set comprises 261 non-overlapping patches from 2024 NAIP imagery, aligned with our SR test locations.
- **Task:** We evaluate whether super-resolved imagery preserves the fine-grained spectral and textural cues necessary for accurate Iceplant delineation, comparing segmentation performance (IoU) across SR outputs and the original high-resolution ground truth.

| Dataset | Split | Patches | Patch Size |
|----------------|--------------|---------|------------|
| NAIP SR (2024) | Train | 236,633 | 512×512 |
| | Validation | 8,569 | |
| | Test | 3,528 | |
| | Total | 248,730 | |
| Iceplant Segm. | Train (2022) | 4,913 | 128×128 |
| | Test (2024) | 261 | |

Table 1: Summary of dataset statistics. The table details the number of patches and dimensions for the NAIP Super-Resolution training set and the Iceplant segmentation downstream task.

4.2 Evaluation Framework

We evaluate our method using a comprehensive protocol that assesses pixel-level fidelity, perceptual quality, and downstream utility. A key feature of our evaluation is that it is performed on whole-image reconstructions rather than individual patches. The entire SR image is generated first, and then metrics are computed on the full scene.

Pixel-wise Accuracy To measure reconstruction fidelity, we employ Root Mean Square Error (RMSE) and Peak Signal-to-Noise Ratio (PSNR). Let I_{HR} and I_{SR} denote the ground truth and super-resolved images with N pixels.

$$\text{RMSE} = \sqrt{\frac{1}{N} \sum_{i=1}^N (I_{HR}^{(i)} - I_{SR}^{(i)})^2} \quad (8)$$

$$\text{PSNR} = 10 \cdot \log_{10} \left(\frac{\text{MAX}_I^2}{\text{MSE}} \right) \quad (9)$$

where MAX_I is the maximum possible pixel value. Additionally, we use the Structural Similarity Index (SSIM) [13] to evaluate structural consistency:

$$\text{SSIM}(x, y) = \frac{(2\mu_x\mu_y + C_1)(2\sigma_{xy} + C_2)}{(\mu_x^2 + \mu_y^2 + C_1)(\sigma_x^2 + \sigma_y^2 + C_2)} \quad (10)$$

where μ and σ represent the mean and variance of intensity, and σ_{xy} is the covariance.

Visual Plausibility Generative models often improve texture at the cost of pixel alignment. To assess perceptual quality, we use the Fréchet Inception Distance (FID) [4] and Kernel Inception Distance (KID) [1]. Since these metrics require an Inception-v3 model [11] to extract feature embeddings, we split the whole-image into patches of size 299×299 with 75% overlap to construct both reference and SR image sets. FID measures the Wasserstein-2 distance between feature distributions of real (r) and generated (g) images:

$$\text{FID} = \|\mu_r - \mu_g\|_2^2 + \text{Tr}(\Sigma_r + \Sigma_g - 2(\Sigma_r \Sigma_g)^{1/2}) \quad (11)$$

where (μ, Σ) denotes the mean and covariance of features. KID calculates the squared Maximum Mean Discrepancy (MMD) between feature representations:

$$\text{KID} = \mathbb{E}[k(x, x')] + \mathbb{E}[k(y, y')] - 2\mathbb{E}[k(x, y)] \quad (12)$$

where $k(\cdot, \cdot)$ is a polynomial kernel used to measure similarity. Both FID and KID are calculated using the `clean-fid` library [6], which addresses aliasing issues during image resizing.

Downstream Performance We evaluate the practical utility of super-resolved imagery through a semantic segmentation task targeting *Carpobrotus edulis* (Iceplant) detection. Effective monitoring and eradication of this aggressive invasive species demands spatially accurate, high-resolution mapping—precisely the capability that our SR framework aims to provide. This task therefore serves as a stringent, application-driven benchmark: it directly tests whether the fine-grained spectral and textural details synthesized by InfScene-SR are sufficiently faithful to support automated ecological analysis, or whether they introduce artifacts that degrade classification accuracy. We employ a U-Net [8] architecture with a ResNet-152 [3] backbone as the segmentation model.

To generate a seamless, full-scene segmentation map, we employ a sliding window inference strategy with significantly overlapping patches. Naively stitching non-overlapping predictions often introduces blocking artifacts at patch boundaries, as convolutional networks typically exhibit degraded performance near the edges where spatial context is limited. To address this, we process the high-resolution input using a patch size of $S \times S$ (where $S = 128$) and a stride of 32 pixels. A 2D Gaussian weighting window $W(i, j)$ is applied to the predicted probability map of each patch before accumulation. The weight for a pixel (i, j) within a patch is defined as:

$$W(i, j) = \exp\left(-\frac{(i - S/2)^2 + (j - S/2)^2}{2\sigma^2}\right) \quad (13)$$

where $\sigma = S/4$. This weighting creates a soft blending effect by assigning higher importance to the central pixels—where predictions are generally more reliable—and suppressing contributions from the patch edges. The final probability map P_{final} at image coordinates (u, v) is obtained by normalizing the accumulated weighted predictions:

$$P_{\text{final}}(u, v) = \frac{\sum_k P_k(u, v) \cdot W_k(u, v)}{\sum_k W_k(u, v)} \quad (14)$$

where P_k is the prediction from the k -th patch and W_k represents the Gaussian window positioned corresponding to that patch.

To comprehensively evaluate the segmentation performance, we report standard classification metrics including Accuracy, Precision, Recall, and F1 Score. Additionally, we use Intersection over Union (IoU) as a primary measure of spatial overlap:

$$\text{IoU} = \frac{\text{TP}}{\text{TP} + \text{FP} + \text{FN}} \quad (15)$$

where TP, FP, and FN represent true positives, false positives, and false negatives, respectively.

4.3 Implementation Details

SR Model Training We adopt the SR3 [9] architecture as our generative backbone, employing a conditional UNet with channel multipliers [1, 2, 4, 8, 16], 64 base channels, group normalization with 16 groups, and a single residual block per resolution level. The network takes as input the concatenation of the low-resolution condition and the noisy image ($2C$ channels) and predicts the noise component (C channels). Weights are initialized with orthogonal initialization, and the model is trained with an L1 loss on the predicted noise.

The forward diffusion process uses a linear noise schedule with β linearly spaced from 10^{-6} to 10^{-2} over $T=2000$ timesteps. We optimize with AdamW using a learning rate of 10^{-4} and weight decay of 10^{-2} . The model is trained for 100 epochs with a batch size of 8 on 512×512 patches, on two NVIDIA L4 GPUs (24 GB VRAM each), leveraging `torch.compile` and mixed-precision training (bf16) for efficiency. Low-resolution inputs are synthesized by downsampling with `cv2.INTER_AREA` to avoid spatial shifting, followed by `cv2.INTER_CUBIC` upsampling to match the target dimensions.

Iceplant Segmentation Training For the downstream semantic segmentation task, we employ a U-Net architecture with a ResNet152 backbone. The model is trained for 100 epochs with a batch size of 64. We use the AdamW optimizer with an initial learning rate of 0.01 and an ExponentialLR scheduler ($\gamma = 0.97$). The training dataset consists of 4,913 patches of size 128×128 , extracted from 2022 NAIP imagery with a stride of 32 pixels.

| Model | RMSE↓ | PSNR↑ | SSIM↑ | FID↓ | KID↓ |
|-------------|---------|---------|--------|---------|--------|
| Bicubic | 9.2889 | 28.7716 | 0.7153 | 90.1341 | 0.0721 |
| SR3 | 37.0532 | 16.7543 | 0.5783 | 69.3676 | 0.0432 |
| InfScene-SR | 24.8974 | 20.2077 | 0.6357 | 33.0953 | 0.0117 |

Table 2: Quantitative reconstruction evaluation. Comparison of pixel-wise fidelity (RMSE, PSNR, SSIM) and perceptual quality (FID, KID) between Bicubic, SR3, and InfScene-SR methods.

5 Results

We present the quantitative and qualitative performance of InfScene-SR compared to the standard patch-based SR3 implementation and the Bicubic interpolation baseline.

5.1 Quantitative Evaluation

Table 2 summarizes the reconstruction fidelity and perceptual quality metrics.

Reconstruction vs. Perception As observed in previous super-resolution literature, there is often a trade-off between distortion metrics (PSNR, SSIM) and perceptual metrics (FID, KID). Bicubic interpolation achieves the highest PSNR (28.77 dB) and SSIM (0.7153) because it acts as a conservative low-pass filter, minimizing pixel-wise squared error. However, this comes at the cost of high-frequency detail, resulting in significantly worse perceptual scores (FID 90.13).

Standard SR3 generates realistic textures but suffers from severe boundary artifacts when applied to large scenes via independent patching, leading to the worst RMSE (37.05) and PSNR (16.75). Incorporating our proposed fusion mechanism, InfScene-SR significantly reduces reconstruction error compared to the baseline SR3 (RMSE from 37.05 to 24.89) while maintaining the generative capability.

Most importantly, InfScene-SR achieves the best perceptual quality, obtaining the lowest FID (33.09) and KID (0.0117). This demonstrates that our method generates imagery that is statistically closest to the real high-resolution distribution, effectively balancing structural consistency with textural fidelity.

| Model | Accuracy \uparrow | Precision \uparrow | Recall \uparrow | F1 Score \uparrow | IoU \uparrow |
|-------------|---------------------|----------------------|-------------------|---------------------|----------------|
| HR | 0.9112 | 0.8365 | 0.8894 | 0.8621 | 0.7577 |
| Bicubic | 0.8948 | 0.7972 | 0.8892 | 0.8407 | 0.7252 |
| SR3 | 0.8792 | 0.7982 | 0.8207 | 0.8093 | 0.6797 |
| InfScene-SR | 0.9101 | 0.8627 | 0.8467 | 0.8546 | 0.7461 |

Table 3: Segmentation performance on the Iceplant dataset. We report classification metrics (Accuracy, Precision, Recall, F1) and Intersection over Union (IoU) to assess the utility of super-resolved images for land cover mapping.

5.2 Qualitative Comparison

Figure 1 visually compares the methods. Bicubic interpolation produces overly smooth and blurry results, failing to resolve fine structures like vegetation texture. The standard SR3 model recovers high-frequency details but exhibits visible grid-like artifacting at patch boundaries, disrupting the visual coherence of the scene. InfScene-SR successfully synthesizes spatially continuous high-resolution details, eliminating seam artifacts while preserving the realistic textures characteristic of diffusion models.

5.3 Downstream Task Performance

The practical utility of the super-resolved images is evaluated via the Iceplant semantic segmentation task (Table 3).

Using original HR imagery sets the upper bound for performance with an IoU of 0.7577 and F1 Score of 0.8621. The artifacts introduced by the standard SR3 model degrade segmentation performance significantly (IoU 0.6797), likely because disjointed boundaries mislead the contextual understanding of the segmentation network.

InfScene-SR recovers performance nearly matching the ground truth, achieving an IoU of 0.7461 and an F1 Score of 0.8546. It outperforms the Bicubic baseline (IoU 0.7252), indicating that the hallucinated details are not merely visual noise but contain semantically meaningful features that aid in accurate land cover classification. Figure 6 illustrates this, showing that InfScene-SR produces segmentation maps with boundary precision comparable to those derived from native high-resolution imagery.

6 Conclusion

In this paper, we introduced InfScene-SR, a novel framework for arbitrary-scale image super-resolution using diffusion models. By addressing the limitations of independent patch processing, we proposed a Memory-Decoupled Accumulation (MDA) strategy integrated with guided and variance-corrected fusion. This approach enables the generation of gigapixel-scale, spatially continuous high-resolution imagery without the seams inherent in standard patch-based inference.

Our comprehensive evaluation demonstrates that InfScene-SR surpasses standard diffusion implementations in both pixel-level fidelity and perceptual quality (FID/KID). Furthermore, we validated the practical value of our method through a downstream semantic segmentation task, where InfScene-SR restored performance to near ground-truth levels, significantly outperforming distinct patch-based approaches. These results suggest that InfScene-SR offers a viable pipeline for enhancing large-scale geospatial imagery, bridging the gap between generative model capability and real-world scalability requirements.

Acknowledgements

The work presented in this paper was supported by the National Science Foundation, United States (No. 2126315, No. 2428775, and No. 2514552).

References

1. Bińkowski, M., Sutherland, D.J., Arbel, M., Gretton, A.: Demystifying MMD GANs. In: International Conference on Learning Representations (Feb 2018), <https://openreview.net/forum?id=r1lUozWCW>
2. Goodfellow, I., Pouget-Abadie, J., Mirza, M., Xu, B., Warde-Farley, D., Ozair, S., Courville, A., Bengio, Y.: Generative adversarial nets. In: Advances in neural information processing systems. pp. 2672–2680 (2014)

3. He, K., Zhang, X., Ren, S., Sun, J.: Deep Residual Learning for Image Recognition. pp. 770–778 (2016), https://openaccess.thecvf.com/content_cvpr_2016/html/He_Deep_Residual_Learning_CVPR_2016_paper.html
4. Heusel, M., Ramsauer, H., Unterthiner, T., Nessler, B., Hochreiter, S.: Gans trained by a two time-scale update rule converge to a local nash equilibrium. *Advances in neural information processing systems* **30** (2017), <https://proceedings.neurips.cc/paper/2017/hash/8a1d694707eb0fefe65871369074926d-Abstract.html>
5. Ho, J., Jain, A., Abbeel, P.: Denoising diffusion probabilistic models. *Advances in neural information processing systems* **33**, 6840–6851 (2020), <https://proceedings.neurips.cc/paper/2020/hash/4c5bcfec8584af0d967f1ab10179ca4b-Abstract.html>
6. Parmar, G., Zhang, R., Zhu, J.Y.: On Aliased Resizing and Surprising Subtleties in GAN Evaluation. In: *Proceedings of the IEEE/CVF Conference on Computer Vision and Pattern Recognition (CVPR)*. pp. 11410–11420 (2022), https://openaccess.thecvf.com/content/CVPR2022/html/Parmar_On_Aliased_Resizing_and_Surprising_Subtleties_in_GAN_Evaluation_CVPR_2022_paper.html
7. Planet Labs PBC: Planet application program interface: In space for life on earth (2017), <https://api.planet.com>
8. Ronneberger, O., Fischer, P., Brox, T.: U-Net: Convolutional Networks for Biomedical Image Segmentation. In: Navab, N., Hornegger, J., Wells, W.M., Frangi, A.F. (eds.) *Medical Image Computing and Computer-Assisted Intervention – MICCAI 2015*. pp. 234–241. *Lecture Notes in Computer Science*, Springer International Publishing, Cham (2015). https://doi.org/10.1007/978-3-319-24574-4_28
9. Saharia, C., Ho, J., Chan, W., Salimans, T., Fleet, D.J., Norouzi, M.: Image Super-Resolution via Iterative Refinement. *IEEE Transactions on Pattern Analysis and Machine Intelligence* **45**(4), 4713–4726 (Apr 2023). <https://doi.org/10.1109/TPAMI.2022.3204461>, <https://ieeexplore.ieee.org/abstract/document/9887996>, conference Name: *IEEE Transactions on Pattern Analysis and Machine Intelligence*
10. Sun, S., Xian, M., Yao, T., Xu, F., Capriotti, L.: Guided and Variance-Corrected Fusion with One-shot Style Alignment for Large-Content Image Generation. *Proceedings of the AAAI Conference on Artificial Intelligence* **39**(7), 7114–7121 (Apr 2025). <https://doi.org/10.1609/aaai.v39i7.32764>, <https://ojs.aaai.org/index.php/AAAI/article/view/32764>, number: 7
11. Szegedy, C., Vanhoucke, V., Ioffe, S., Shlens, J., Wojna, Z.: Rethinking the inception architecture for computer vision. In: *Proceedings of the IEEE conference on computer vision and pattern recognition*. pp. 2818–2826 (2016), https://www.cv-foundation.org/openaccess/content_cvpr_2016/html/Szegedy_Rethinking_the_Inception_CVPR_2016_paper.html
12. USDA Farm Service Agency: National agriculture imagery program (NAIP) (2024)
13. Wang, Z., Bovik, A., Sheikh, H., Simoncelli, E.: Image quality assessment: from error visibility to structural similarity. *IEEE Transactions on Image Processing* **13**(4), 600–612 (Apr 2004). <https://doi.org/10.1109/TIP.2003.819861>, <https://ieeexplore.ieee.org/document/1284395>